EPJ AP

Applied Physics

EPJ.org

your physics journal

Eur. Phys. J. Appl. Phys. (2016) 73: 30401 DOI: 10.1051/epjap/2016150539

Effect of Fe doping on the electrical and magnetic properties of $Sn_{1-x}Fe_xO_2$ nanoparticles

Saleh A. Saleh, Ahmed M. Abdel Hakeem, and Eslam M.M. Ibrahim

edp sciences

The title "The European Physical Journal" is a joint property of EDP Sciences, Società Italiana di Fisica (SIF) and Springer

Eur. Phys. J. Appl. Phys. (2016) 73: 30401
DOI: 10.1051/epjap/2016150539

THE EUROPEAN PHYSICAL JOURNAL APPLIED PHYSICS

Regular Article

Effect of Fe doping on the electrical and magnetic properties of $Sn_{1-x}Fe_xO_2$ nanoparticles

Saleh A. Saleh[1,2], Ahmed M. Abdel Hakeem[1,a], and Eslam M.M. Ibrahim[1]

[1] Physics Department, Faculty of Science, Sohag University, 82524 Sohag, Egypt
[2] Physics Department, College of Science & Arts, Najran University, P.O. Box 1988 Najran, Saudi Arabia

Received: 29 October 2015 / Received in final form: 1 February 2016 / Accepted: 4 February 2016
Published online: 9 March 2016 –

Abstract. In this work, $Sn_{1-x}Fe_xO_2$ ($x = 0.00$, 0.02, 0.04, 0.06 and 0.08) nanoparticles have been synthesized using ball-milling method. The average diameter of the nanoparticles decreases from 487 to 216 nm by adding Fe_2O_3 to the tin dioxide. The X-ray diffraction analyses confirms formation of tetragonal structure which is typical feature of SnO_2 compounds. Theoretical density was found to be larger than the corresponding physical one due to the porosity of the materials. The electrical resistivity versus temperature measurements confirm that the undoped and Fe doped SnO_2 nanoparticles are characterized with semiconducting behavior over the whole measurement range of temperature 300–473 K. The magnetic measurements confirm transformation from diamagnetic to ferromagnetic characteristics as Fe doping level reaches $x = 0.06$.

1 Introduction

Metal oxides attract great interest of enormous research groups because of the broad range of their important technological properties [1–17]. Particularly, tin dioxide (SnO_2) presents itself as one of the promising materials where it possesses various properties suitable for fabrication of different efficient electronics and optoelectronics devices such as transparent conducting electrodes [1,2], solar cells [3], photocatalysis [4,5] and so on. Additionally, SnO_2 has received considerable attention as solid-state gas sensors because of its chemical and thermal stability, natural non-stoichiometry and stable rutile phase [6–15]. Working as gas sensors is based on the chemical reaction caused by adsorption of the gas on the SnO_2 surface and the resulted change of the electrical conductance [16,17].

Tin dioxide is a wide band gap n-type semiconductor (of 3.6 eV) [1]. Considerable experimental investigations focus on the synthesis of SnO_2 and tuning of its band gap by various doping and alloying methods. It has been recently confirmed that the sensibility and response of SnO_2 gas sensors could be improved by the use of appropriate additives and processing methods [18]. This is reasonable because incorporation of impurities or defects into semiconductor lattices are vital means for tailoring electrical resistivity of the semiconductor [19–23]. Iron is a particularly interesting element for doping SnO_2 because Fe^{3+} is a lower valence cation and thus can vary the Debye length through changing the carrier concentration. Therefore, by controlling Fe content, the electrical properties of SnO_2 can be tuned and feasibility of using as gas-sensors can be improved [24].

$Sn_{1-x}Fe_xO_2$ nanostructures have been successfully synthesized by various techniques, such as sol-gel, ball milling, hydrothermal methods and polymeric precursors method [25–33]. Among them, the ball milling carries a number of advantages it is a fast, simple, low-cost and low-maintenance technique with a few drawbacks like impurities, disorders and defects introduced in the material. Ribeiro et al. discussed deeply the role of milling time on the impurities contents in the $Sn_{1-x}Fe_xO_2$ composition. They showed that the complete incorporation of Fe_2O_3 by SnO_2 occurs not before 3 h of milling as was confirmed by the Mössbauer spectroscopy [34].

Study of the bulk Fe doped SnO_2 materials have been reported by many research groups while their properties in nanosized scale are not fully explored. This work presents a study of the effect of Fe doping on the structural, electrical and magnetic properties of tin dioxide particles synthesized in nano-sized scale. Fabrication of gas-sensor devices with tiny particles size improves significantly the sensibility of gas detection since the surface to volume ratio becomes much larger. Noteworthy, the electrical properties of the tiny particles of a semiconductor exhibits large deviation from those of single-crystalline or bulk polycrystalline counterparts [35]. Deviation of the electrical properties comes from the band structure modification, the quantum confinement of the charge carriers and the

[a] e-mail: ahmedhakeem75@yahoo.com

predominant contribution of the largely defective and strained grain boundaries resulted from decreases of the particles size to nanometer scale.

2 Experimental details

Samples of chemical formula $Sn_{1-x}Fe_xO_2$ ($x = 0.00$, 0.02, 0.04, 0.06 and 0.08) were prepared from high purity oxides (SnO_2 and Fe_2O_3). The precursors were weighed and mixed according to the desired stoichiometry and then ball milled for 2 h. The powder mixtures were gone into conventional solid-state technique where they were pressed at room temperature into pellets inside a stainless steel die under 5 ton cm^{-2} and subsequently sintered in air at 1423 K for 24 h. After that, the materials were ball milled for 12 h at a rotation speed of 300 rpm with ethylene.

Phase analysis was done by means of X-ray diffraction (XRD) using a PANalytical X'Pert PRO diffractometer at room temperature with Cu (Kα) radiation ($\lambda = 1.5406$ Å). A 2θ scan was taken from 10° to 90° with a sampling pitch of 0.02°. The morphology of the samples was studied by a field emission scanning electron microscope (FE-SEM: JEOL JSM-7600F) techniques. Composition analysis was carried out using energy dispersive spectroscopy (EDS) attached to the FE-SEM. The electrical resistivity was carried out at various temperature ranging from room temperature to 473 K in a vacuum of 10^{-3} mmHg which was found to contribute much to the thermal stability during measurements. A DC voltage (1.1 V) was applied across the sample and the resulted current was measured by a digital picoammeter (DPM-111 Scientific Equipments, Roorkee). The temperature was measured by a calibrated copper-constantan thermocouple mounted near the sample. The magnetic properties were studied using a commercial superconducting quantum interference device magnetometer (VSM-SQUID).

3 Results and discussion

3.1 Structural studies

Figure 1 shows the XRD patterns of the pure and Fe-doped SnO_2 samples. The diffraction peaks are corresponding to typical tetragonal structure of SnO_2 alloys phases (PDF code: 00-041-1445) with space group *P42/mnm* (136) confirming the expected crystal structure. Variation of some peaks intensities with changing the doping concentration can be observed.

The sharpness of the peaks indicates to the well crystallinity of the prepared sample. Noteworthy, no indications of peaks corresponding to impurity phases or other tin- or iron-oxides phases were detected. Also, no peaks were detected for the Fe-Sn oxide phase even for the most Fe doped SnO_2 sample. This may be reasonable because formation of such phase requires low cooling rate, high synthetic pressure, and high dopant concentration, which are not realized in this work [36].

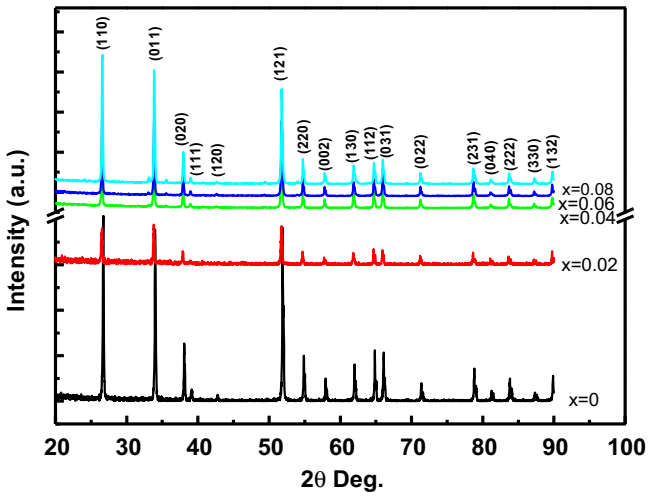

Fig. 1. XRD patterns of pure and Fe-doped SnO_2 samples.

Assuming that the nanoparticles have spherical shape and according to the well-known Scherrer's equation [37]: $C_s = \frac{0.89\lambda}{\beta \cos\theta}$, the crystallite size of the nanoparticles can be calculated from the full width of half maximum β of the diffraction peak corresponding to the Bragg's angle θ. Taking into account the wavelength of Cu Kα radiation $\lambda = 1.5418$ Å yields the mean diameter C_s equal to 180 nm of the pure SnO_2 samples and decreases sequentially by increasing the Fe content to reach 92.2 nm for the sample of $x = 0.08$ (see Tab. 1).

For tetragonal structure, the lattice parameters a and c are calculated using the relations [38]:

$$a = \left(\frac{(h_2^2 + k_2^2) l_1^2 - (h_1^2 + k_1^2) l_2^2}{l_1^2 d_1^2 - l_2^2 d_2^2} \right)^{0.5} \times d_1 d_2,$$

$$c = \left(1 - \left(\left(\left(h_1^2 + k_1^2\right) d_1^2\right) / a^2\right)\right)^{-0.5}.$$

The data tabulated in Table 1 shows that the lattice parameters are nearly constant with variation of the Fe content in the SnO_2 samples. The unchanged values of a and c likely arises from the following reasons: (i) the relatively low content of Fe_2O_3 in the compounds and (ii) the low change of defects amounts caused by the oxygen content in the sample due to also the relatively low content of Fe_2O_3 [39]. Noteworthy, the unchanged values of the lattice parameters indicate well incorporation of Fe into the SnO_2 host lattice. This matches well with the monophase feature observed from the XRD patterns and the complete absence of the iron oxide as second phase. Similar behavior has been reported in other works [40].

It is well known that density plays a key role in controlling the properties of polycrystalline oxides [41]. Therefore, the samples density was determined by two different methods. Firstly, the physical density (ρ_P) of each sample was measured by the formula $\rho_P = \frac{m}{\pi r^2 h}$ where m is the mass, r is the radius and h is the vertical height of the sample in pellet form. Secondly, the theoretical density, ρ_{th}, was evaluated by substituting the value of the lattice

Table 1. Structural properties of the synthesized samples.

x%	C_s (nm)	a (Å)	c (Å)	c/a	ρ_{th} (g cm^{-3})	P_p (g cm^{-3})	Porosity	d_{SEM} (nm)
0.00	180	4.72	3.18	0.67	7.02	2.6	63.0	633
0.02	161.25	4.75	3.18	0.67	6.89	5.4	21.3	528
0.04	92.5	4.75	3.19	0.67	6.79	5.2	23.2	468
0.06	92.5	4.75	3.19	0.67	6.74	4.6	31.6	411
0.08	92.2	4.74	3.19	0.6722	6.70	4.8	28.5	385

parameters a and c in the following formula:

$$\rho_{th} = \frac{ZM}{N_A a^2 c},$$

where Z, M andN_A are the number of molecules in the unit cell, the molar mass and the Avogadro's number, respectively. The values of ρ_P and ρ_{th} are presented in Table 1. The data reveal that theoretical density ρ_{th} decreases as the Fe content increases while the physical density doesn't show sequential change. This may be attributed to existence of pores in the samples which makes calculation of physical density not so accurate. Existence of porosity may also be the reason of why theoretical density of each sample is larger than the corresponding physical one. To estimate the porosity of the samples, the following formula was employed [42]:

$$P = \left(1 - \frac{\rho_p}{\rho_{th}}\right) \times 100,$$

where ρ_P is the physical density and ρ_{th} is the theoretical density. From Table 1, the porosity values do not vary sequentially as the Fe increases in the samples and this may explain the non-sequential change of the physical density values mentioned above.

3.2 Morphological studies

Figure 2 shows scanning electron microscope (SEM) images of $Sn_{1-x}Fe_xO_2$ ($x = 0.00, 0.02, 0.04, 0.06$ and 0.08) samples. Generally, the samples consist of nano-sized semispherical particles. Note that, no significant differences in the overall morphology of the samples were observed.

The average size d_{SEM} of the particles were determined by counting 100 particles at different locations at each sample surface. The results of this analysis are displayed in histograms depicted as insets in Figure 2. The data imply that d_{SEM} decreases from 487 to 216 nm by adding Fe_2O_3 to the tin dioxide. Notably, d_{SEM} is much larger than the crystallite size C_s calculated from XRD (see Tab. 1) since the former represents the size of aggregated nanocrystallites of $Sn_{1-x}Fe_xO_2$. However, both of them show the same trend with increasing the Fe concentration in the samples. All the materials were investigated by the energy dispersive X-ray EDX spectrometer. It was found that the materials composition matches well with the desired stoichiometry. Noteworthy, analyzing several different locations of each material confirms that the material is of the same chemical composition, which confirm the good homogeneity of the prepared samples.

3.3 DC electrical resistivity

The temperature dependence of electrical resistivity (ρ) was measured in the range between 300 and 473 K. Figure 3 shows the ρ-T plots for the samples of $0.00 \leq x \leq 0.08$. The undoped sample show typical behavior of semiconductor over the whole range of temperature (see the inset of Fig. 3).

However, for Fe-doped SnO_2 samples, the conduction behavior is featured by two distinct mechanisms where ρ-T plot consists of two distinct regions around a certain transition temperature T_p. It was found that, the T_p value increases significantly as the Fe content increases in the samples (see Tab. 2). In the low temperature region ($300\ K \leq T \leq T_p$), the resistivity is relatively constant as the temperature of measurement increases. The constant ρ-T behavior can be attributed to the free carriers created due to the Fe incorporation in the SnO_2 lattice and thus the associated mobility dependence conduction mechanism. From this behavior, one can conclude that the low temperature region is characterized by a competition between the carrier mobility and thermal activation mechanisms. The contribution of the carrier mobility mechanism due to existence of free carriers is the reason of the resistivity increase with the increase of the Fe concentration in the samples. Obviously, the room temperature resistivity $\rho_{300\ K}$ increases with Fe substitution as seen in Figure 4.

The high temperature range ($T_p \leq T \leq 473$ K) is characterized by sudden sharp fall of the resistivity with increasing the temperature. In this range, the electrons are excited above the mobility edge and the thermal activation mechanism of conduction become dominant as a typical feature of semiconductors. The electronic conduction mechanism was found to be well represented by a simple thermal activation law [43]: $\rho(T) = \rho_o \exp(E_\rho / K_\beta T)$ where the pre-exponential factor ρ_o depends on the composition of the samples [44], K_B is the Boltzmann's constant, T is the absolute temperature and E_ρ is the corresponding activation energy, which is a function of the electronic energy levels of chemically interacting atoms in the materials and hence of the emerged band gap. From the plot of $\ln \rho$ versus $1/T$ (Fig. 5), the activation energy E_ρ of all samples is estimated and tabulated in Table 2.

The E_ρ values coincide with those reported previously in other works [4,6]. Besides, they increase as the Fe content increases in the samples which explain the increase of the electrical resistivity by Fe doping.

Figure 6 shows magnetic field (H) dependence of magnetization (M) for the materials at hand. The data exhibit

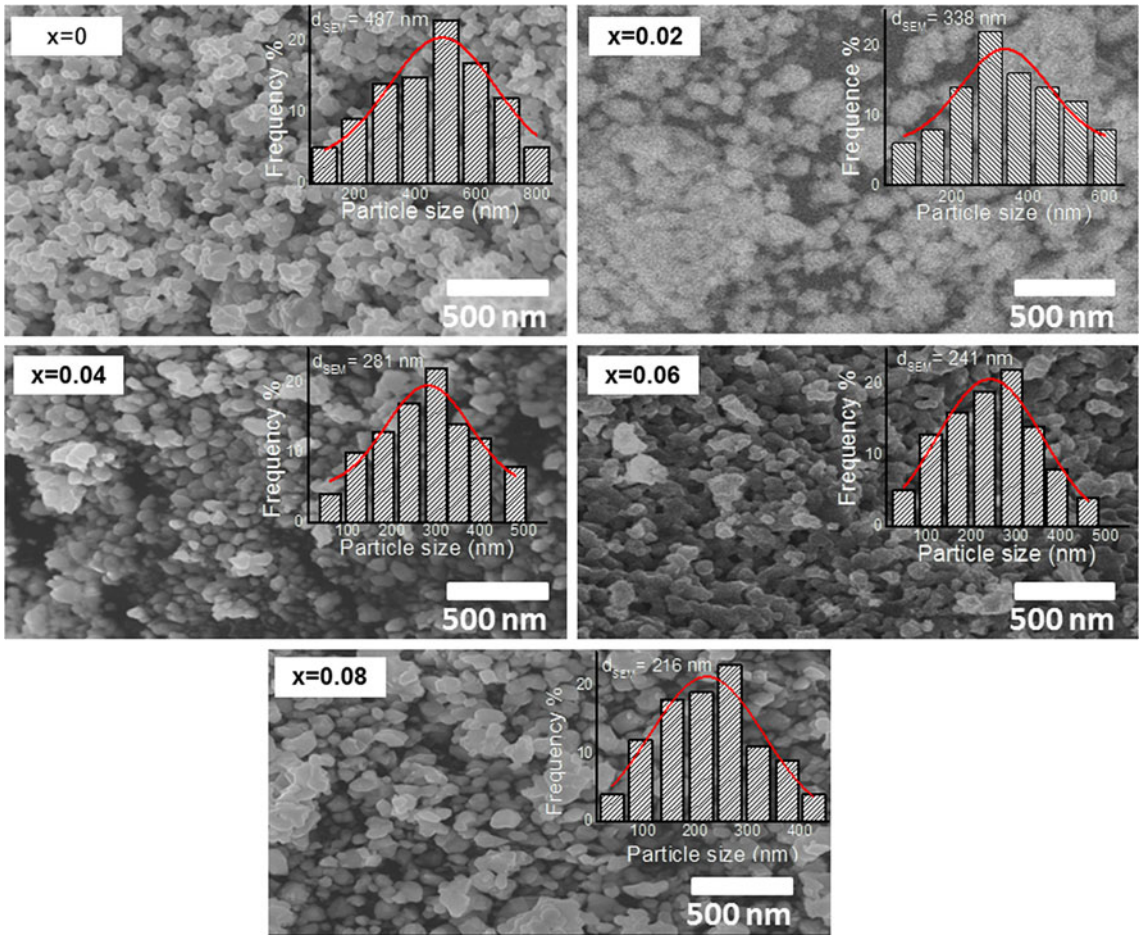

Fig. 2. SEM images of pure and Fe-doped SnO_2 samples.

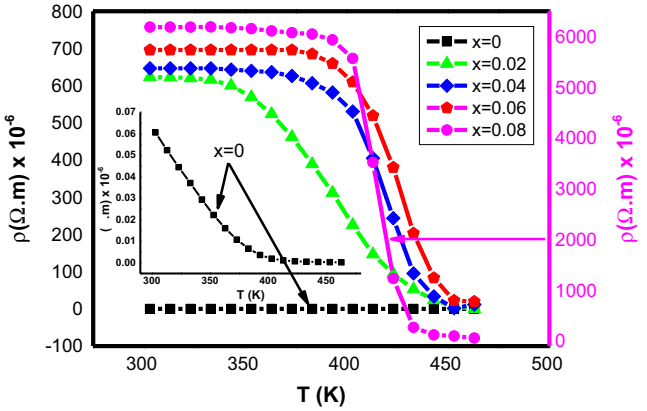

Fig. 3. The temperature dependence of the electrical resistivity for pure and Fe-doped SnO_2 samples.

diamagnetic characteristic with negative magnetic susceptibility for the pure SnO_2 (sample of $x = 0$) as expected. The negative magnetic susceptibility extends to the samples of $x = 0.02$ and 0.04 which may be attributed to the low content of the Fe oxide and domination of the diamagnetic features.

However, the room temperature M versus H plots of these samples are featured with a hysteretic behavior.

Table 2. The transition temperature T_p and the activation energy E_ρ of the $Sn_{1-x}Fe_xO_2$ ($x = 0.00$, 0.02, 0.04, 0.06 and 0.08).

x%	0.00	0.02	0.04	0.06	0.08
T_p (K)	–	348	398	401	403
E_ρ (eV)	0.68	0.87	1.25	1.49	1.59

Further Fe doping changes the magnetic behavior of the $Sn_{1-x}Fe_xO_2$ samples where, as shown in Figure 6, $x = 0.06$ and 0.08 samples possess positive magnetic susceptibility with room temperature ferromagnetic behavior. The most notable thing for these samples is the unsaturation of the M versus H plots which may indicates a strong paramagnetic contribution at higher magnetic field [45]. The coercivity (H_c) is 5983 and 6620 Oe while the retentivity (M_r) is 0.013 and 0.019 emu/g for the samples of $x = 0.06$ and 0.08, respectively. The room temperature ferromagnetic behavior appears at doping level $x = 0.6$ might suggest a major role of surface oxygen vacancies and charge carriers with taking in consideration the model proposed by Coey et al. [46]. for ferromagnetism in oxide semiconductors. According to this mode, the transition metal dopants act as charge reservoirs from which electrons can be transferred to local defect

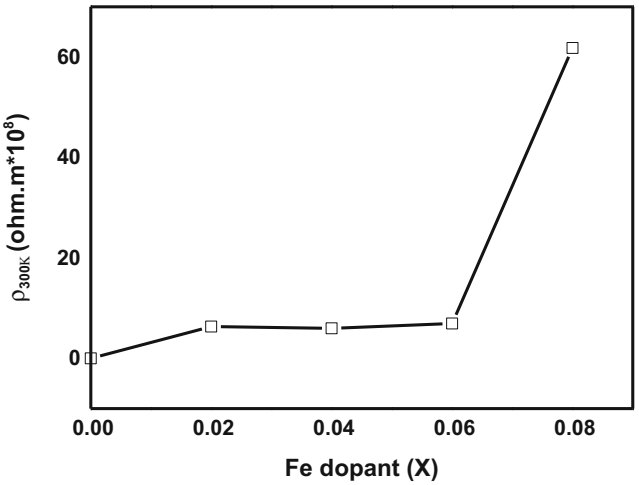

Fig. 4. The Fe concentration dependence of electrical resistivity, at 303 K for pure and Fe-doped SnO_2 samples.

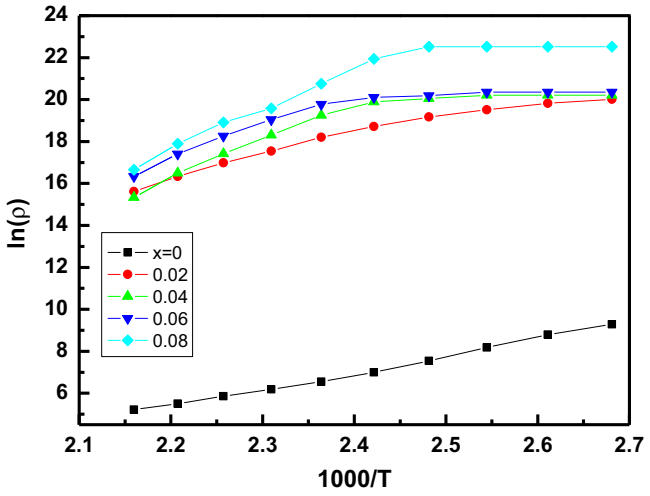

Fig. 5. The plots of $\ln \rho$ versus 1000/T for pure and Fe-doped SnO_2 samples.

density of states such as oxygen vacancies in a nanoparticle which could raise the Fermi level to fulfill the Stoner criterion condition of ferromagnetism. If the energy needed for the charge transfer is lower than the energy gained from spin splitting, surface states could develop a magnetic moment and the surface shell of the nanoparticle that is rich in oxygen vacancies can spontaneously order ferromagnetically [47].

4 Conclusion

A study on structural, and electrical resistivity of polycrystalline $Sn_{1-x}Fe_xO_2$ (x = 0.00, 0.02, 0.04, 0.06 and 0.08) compounds have been carried out. We investigated the effects of iron concentration on the densification, electrical properties and magnetic features of $Sn_{1-x}Fe_xO_2$ (x = 0.00, 0.02, 0.04, 0.06 and 0.08) ceramics prepared by the solid state reaction method. XRD patterns of all samples showed only peaks characteristic of cassiterite

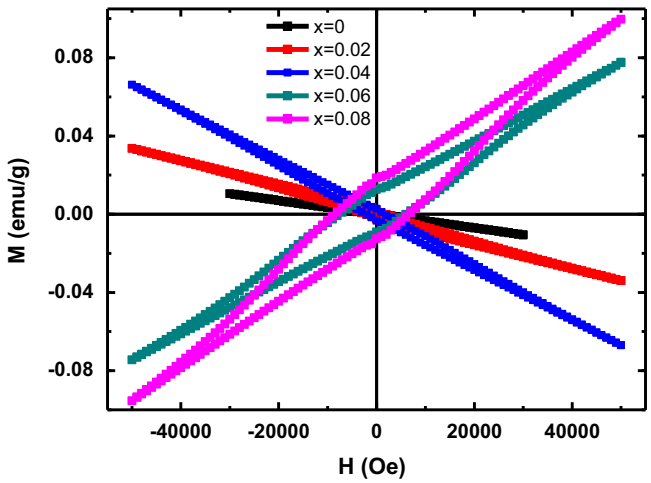

Fig. 6. Magnetization versus magnetic field plots of the $Sn_{1-x}Fe_xO_2$ (x = 0.00, 0.02, 0.04, 0.06 and 0.08) measured at room temperature.

phase SnO_2. The microstructure study confirmed decrease of grain size with Fe doping which coincides with the XRD data. The pure SnO_2 sample was characterized by typical semiconductor behavior over the whole temperature of measurement. However, the Fe-doped samples were featured by a transition between two distinct conduction mechanisms around a certain transition temperature. The low temperature region showed competition between carrier mobility and semiconductor conduction mechanisms while with elevating the measurement temperature, the semiconductor mechanism dominated. The magnetic measurements revealed that the the $Sn_{1-x}Fe_xO_2$ (x = 0.00, 0.02 and 0.04) are diamagnetic materials. However, the x = 0.06 and 0.08 samples are ferromagnetic with coercivity 5983 and 6620 Oe, respectively.

References

1. R.K. Mishra, P.P. Sahay, Mater. Res. Bull. **47**, 4112 (2012)
2. S.A. Saleh, S.A. Ahmed, E.M.M. Elsheikh, J. Supercond. Nov. Magn. **21**, 187 (2008)
3. A.Y. El-Etre, S.M. Reda, Appl. Surf. Sci. **256**, 6601 (2010)
4. B. Esen, T. Yumak, A. Sinag, T. Yildiz, Photochem. Photobiol. **87**, 267 (2011)
5. G. Cheng, J. Chen, H. Ke, J. Shang, R. Chu, Mater. Lett. **65**, 3327 (2011)
6. G. Xi, J. Ye, Inorg. Chem. **49**, 2302 (2010)
7. F. Gyger et al., Chem. Mater. **22**, 4821 (2010)
8. L.A. Patil et al., Curr. Appl. Phys. **10**, 1249 (2010)
9. S. Liu et al., Mater. Chem. Phys. **123**, 109 (2010)
10. M. Morimitsu et al., Sens. Actuators B **67**, 184 (2000)
11. Y.-S. Choe, Sens. Actuators B **77**, 200 (2001)
12. B.-Y. Wei et al., Sens. Actuators B **101**, 81 (2004)
13. H.C. Wang, Y. Li, M.J. Yang, Sens. Actuators B **119**, 380 (2006)
14. G. Korotcenkov, B.K. Cho, Sens. Actuators B **142**, 321 (2009)
15. I. Kocemba, J. Rynkowski, Sens. Actuators B **155**, 659 (2011)

16. Z. Chen, J.K.L. Lai, C.H. Shek, H. Chen, J. Mater. Res. **18**, 1289 (2003)
17. S.A. Saleh, S.M. Khalil, E.M.M. Ibrahim, Supercond. Sci. Technol. **20**, 372 (2007)
18. M.A. Ponce, R. Parra, M.S. Castro, C.M. Aldao, J. Mater. Sci.: Mater. Electron. **18**, 1171 (2007)
19. C. Drake, S. Seal, Appl. Phys. Lett. **90**, 233117 (2007)
20. H.M. Yang, X. Song, X. Zhang, W. Ao, G. Qiu, Mater. Lett. **57**, 3124 (2003)
21. G. Xu, Y.-W. Zhang, X. Sun, C.-L. Xu, C.-H. Yan, J. Phys. Chem. B **109**, 3269 (2005)
22. A.P. Maciel, P.N. Lisboa-Filho, E.R. Leite, C.O. Paiva-Santos, W.H. Schreiner, Y. Maniette, E. Longo, J. Eur. Ceram. Soc. **23**, 707 (2003)
23. C. Drake, A. Amalu, J. Bernard, S. Seal, J. Appl. Phys. **101**, 104307 (2007)
24. K. Galatsis et al., Sens. Actuators B **93**, 562 (2003)
25. C.E. Rodriguez-Torres, L. Errico, F. Golmar, A.M. Mudarra-Navarro, A.F. Cabrera, S. Duhalde, F.H. Sánchez, M. Weissmann, J. Magn. Magn. Mater. **302**, e219 (2007)
26. A.F. Cabrera, A.M. Mudarra-Navarro, C.E. Rodriguez-Torres, F.H. Sánchez, Physica B **398**, 215 (2007)
27. L.C. Sánchez, J.J. Beltran, J. Osorio, A.M. Calle, C.A. Barrero, Hyperfine Interact. **195**, 185 (2010)
28. L. Fang, X. Zu, C. Liu, Z. Li, G. Peleckis, S. Zhu, H. Liu, L. Wang, J. Alloys Compd. **491**, 679 (2010)
29. M. Sorescu, L. Diamandescu, D. Tarabasanu-Mihaila, V.S. Teodorescu, B.H. Howard, J. Phys. Org. Chem. **65**, 1021 (2004)
30. J.F. Liu, M.F. Lu, P. Chai, L. Fu, Z.L. Wang, X.Q. Cao, J. Menga, J. Magn. Magn. Mater. **317**, 1 (2007)
31. J. Sakuma, K. Nomura, C. Barrero, M. Takeda, Thin Solid Films **515**, 8653 (2007)
32. A. Thurber, K.M. Reddy, A. Punnoose, J. Appl. Phys. **105**, 07E706 (2009)
33. S. Ribeiro-Thiago, M. Sasaki-José, F. Vasconcelos-Igor, J. Mater. Sci. **47**, 2630 (2012)
34. H.S. Nalwa (Ed.), *Handbook of Nanostructured Materials and Nanotechnology* (Academic, USA, 2000)
35. S.A. Ahmed, E.M.M. Ibrahim, S.A. Saleh, Appl. Phys. A **85**, 177 (2006)
36. M.M. Ibrahim, E.M.M. Ibrahim, S.A. Saleh, A.M. Abdel Hakeem, J. Alloys Compd. **429**, 19 (2007)
37. S.A. Saleh, E.M.M. Ibrahim, Philos. Mag. **91**, 841 (2011)
38. S.S. Fouad, G.B. Sakr, I.S. Yahia, D.M. Abdel Basset, Mater. Res. Bull. **46**, 2141 (2011)
39. A. Mahmood, M.F. Warsi, M.N. Ashiq, M. Sher, Mater. Res. Bull. **47**, 4197 (2012)
40. M.M. Bagheri-Mohagheghi et al., Solid State Sci. **11**, 233 (2009)
41. S. Akhter, D.P. Paul, Md. Abdul Hakim, D.K. Saha, Md. Al-Mamun, A. Parveen, Mater. Sci. Appl. **2**, 1675 (2011)
42. M. Rahimi, P. Kameli, M. Ranjbar, H. Hajihashemi, H. Salamati, J. Mater. Sci. **48**, 2969 (2013)
43. S.A. Saleh, A.A. Hendi, I.A. Abdel-Latif, J. American Sci. **7**, 923 (2011)
44. E.M.M. Ibrahim, Appl. Phys. A **89**, 203 (2007)
45. S. Ghosh, M. Mandal, K. Mandal, J. Magn. Magn. Mater. **323**, 1083 (2011)
46. J.M.D. Coey, K. Wongsaprom, J. Alaria, M. Venkatesan, J. Phys. D: Appl. Phys. **41**, 134012 (2008)
47. K. Dodge, J. Chess, J. Eixenberger, G. Alanko, B.H. Charles, A. Punnoose, J. Appl. Phys. **113**, 17B504 (2013)